Earth Surface Processes and Landforms

Quantifying the effect of geomorphology on aeolian dust emission potential in northern China

Journal:	*Earth Surface Processes and Landforms*
Manuscript ID	ESP-18-0242.R2
Wiley - Manuscript type:	Research Article
Date Submitted by the Author:	n/a
Complete List of Authors:	CUI, MENGCHUN; Nanjing University, School of Geography and Ocean Science; University of Oxford, School of Geography and the Environment Lu, Huayu; Nanjing University, School of Geography and Ocean Science Wiggs, Giles; University of Oxford, School of Geography and the Environment Etyemezian, Vicken; Desert Research Institute, Division of Atmospheric Sciences Sweeney, Mark; University of South Dakota, Sustainability & Environment Xu, Zhiwei; Nanjing University, School of Geography and Ocean Science
Keywords:	PM10, dust emission, northern China, seasonality, PI-SWERL

Quantifying the effect of geomorphology on aeolian dust emission potential in northern China

Mengchun Cui[1,2], Huayu Lu[1*], Giles F. S. Wiggs[2], Vicken Etyemezian[3], Mark R. Sweeney[4], Zhiwei Xu[1]

[1]School of Geography and Ocean Science, Nanjing University, Nanjing, China

[2]School of Geography and the Environment, University of Oxford, Oxford, UK

[3]Division of Atmospheric Science, Desert Research Institute, Las Vegas, Nevada, USA

[4]Department of Sustainability & Environment, University of South Dakota, Vermillion, South Dakota, USA

*Correspondence to: Huayu Lu, huayulu@nju.edu.cn. Tel.: +86 25 89680798; fax: +86 25 89682686.

ABSTRACT: Representation of dust sources remains a key challenge in quantifying the dust cycle and its environmental and climatic impacts. Direct measurements of dust fluxes from different landform types are useful in understanding the nature of dust emission and characterizing the dynamics of soil erodibility. In this study we used the PI-SWERL® instrument over a seasonal cycle to quantify the potential for PM_{10} (particles with diameter ≤10 μm) emission from several typical landform types across the Tengger Desert and Mu Us Sandy Land, northern China. Our results indicate sparse grasslands and coppice dunes showed relatively high emission potentials, with emitted fluxes ranging from 10^{-1} to 10^{1} mg m^{-2} s^{-1}. These values were up to five times those emitted from sand dunes, and 1-2 orders of magnitude greater than the emissions from dry lake beds, stone pavements and dense grasslands. Generally, PM_{10} emission fluxes were seen to peak in the spring months, with significant reductions in summer and autumn (by up to 95%), and in winter (by up to 98%). Variations in soil moisture were likely a primary controlling factor responsible for this seasonality in PM_{10} emission. Our data provide a relative quantification of differences in dust emission potential from several key landform types. Such data allow for the evaluation of current dust source schemes proposed by prior researchers. Moreover, our data will allow improvements in properly characterizing the erodibility of dust source regions and hence refine the parameterization of dust emission in climate models.

KEYWORDS: PM_{10}; dust emission; northern China; seasonality; PI-SWERL

Introduction

Dust is a major component of atmospheric global aerosol loading and can exert profound climatic and environmental impacts. Once airborne, dust particles can affect the climate system not only through direct radiative forcing (e.g. Tegen et al., 1996; Evan et al., 2009; Kok et al., 2017), and interaction with clouds (e.g. Yin and Chen, 2007; Karydis et al., 2017), but also through participating in biogeochemical cycles within terrestrial (e.g. Okin et al., 2004; Mahowald et al., 2008) and marine ecosystems (e.g. Jickells et al., 2005; Mahowald et al., 2018) upon deposition. At source, the loss of nutrients and fine particles due to dust emission may result in soil degradation (e.g. Bielders et al., 2002; Katra et al., 2016). Also, dust storms significantly affect regional air quality and human health (e.g. Kellogg and Griffin, 2006; Middleton, 2017). However, the magnitude of global dust emissions remains uncertain, varying from ~500 Tg yr^{-1} to ~4000 Tg yr^{-1} among different models for PM_{10} (e.g. Zender et al., 2003a; Cakmur et al., 2006; Huneeus et al., 2011; Albani et al., 2014; Kok et al., 2017). A key challenge of dust emission estimates is the representation of dust sources in terms of the spatial and temporal dynamics of soil erodibility (Zender et al., 2003b; Cakmur et al., 2006; Kok et al., 2014).

Soil erodibility is highly variable in space and time, depending on soil properties, land surface characteristics and environmental conditions (e.g. Shao, 2008; Webb and Strong, 2011). Given insufficient information on soil properties worldwide, many models typically employ source functions to help account for spatial variations in erodibility through sediment supply (e.g. Ginoux et al., 2001; Zender et al., 2003b), surface reflectance (Grini et al., 2005) or surface morphology (Koven and Fung, 2008). However, differing approaches to determining soil erodibility tend to reveal different areas as prime dust sources. Such variations in identifying source areas transfers further uncertainty into the estimates of global dust emission (Zender et al., 2003b; Grini et al., 2005; Cakmur et al., 2006). Moreover, these time-invariant source functions cannot account for temporal variations in soil erodibility (Zender and Kwon, 2005; Webb and Mcgowan, 2009; Wu et al., 2016). At monthly or seasonal scales, soil erodibility is primarily controlled by sediment availability (rather than sediment supply), which is highly sensitive to dynamic changes in soil moisture and vegetation conditions (Zender and Kwon, 2005).

To address this issue, Bullard et al. (2011) developed a conceptual geomorphic scheme to represent the dynamics of natural dust sources through relating dust emission to geomorphology and sedimentology. This scheme has been evaluated at several active dust sources using satellite remote sensing data (e.g. Bullard et al., 2011; Lee et al., 2012; Baddock et al., 2016; von Holdt et al., 2019). Given the increasingly important role of human impact on soil erodibility, several studies have used satellite-based dust indicators allied with land cover maps to attribute dust emission to natural or anthropogenic sources (Lee et al., 2012; Ginoux et al., 2012; Parajuli et al., 2014). A recent example has combined hydrological processes and geomorphic signatures to collectively represent the geomorphic controls on dust sources (Parajuli and Zender, 2017). While satellite remote sensing is instrumental in identifying the spatial distribution of dust sources, there remain some uncertainties and inaccuracies related to the dust detection algorithms, overpass time, cloud effects and image/signal interpretation (e.g. Baddock et al., 2009; Brindley et al., 2012; Ashpole and Washington, 2013; Parajuli and Zender, 2017). Where possible, it is advantageous to collect in-situ measurements of dust emission from typical landform types as dust emission is a small-scale and stochastic process (Bullard, 2010; Shao et al., 2011). This would enable us to better characterize the dust emission processes and to improve the dust parameterizations in climate models, a requirement for proper examination of the impact of past and future climate change on aerosol loading in the atmosphere (Mahowald et al., 2006; Bullard, 2010; Kok et al., 2018).

In the present study we used a miniaturized wind shear system, the Portable In-Situ Wind ERosion Lab (PI-SWERL), which generates a certain shear stress on the ground surface and allows multiple tests in a short time (Etyemezian et al., 2007; Sweeney et al., 2008). The PI-SWERL has been used to examine the propensity of various landform types for PM_{10} emission, such as sand dunes (e.g. Cui et al., 2015; Sweeney et al., 2016), dry lake beds (e.g. King et al., 2011; Sweeney et al., 2011), fluvial surfaces (e.g. Sankey et al., 2011; von Holdt et al., 2017) and grasslands (e.g. Munkhtsetseg et al., 2016, 2017). These studies have provided insights into the physical processes

104 of dust emission and its dependency on soil characteristics (Bryant, 2013).
105 However, similar quantitative data from northern China are scarce. While
106 several approaches have been used to examine the geomorphic controls on
107 dust sources in northern China, such as particle size and geochemical
108 analyses of surface samples (e.g. Wang et al., 2005, 2008), field passive sand
109 traps (Wang et al., 2015) and laboratory wind tunnel measurements (Wang et
110 al., 2017), relatively little attention has focused on the seasonal heterogeneity
111 in dust emissions. Following our pilot work (Cui et al., 2015; Sweeney et al.,
112 2016), we used the PI-SWERL to directly measure the PM_{10} emissions from
113 several landform types during different seasons in the Tengger Desert and Mu
114 Us Sandy Land, northern China. These two deserts are located in the
115 transition zone between the northwestern arid deserts, the eastern semi-arid
116 grasslands and the southwest cold mountainous regions of China, which are
117 subjected to both climate change and human activity (Wang et al., 2008; Lu et
118 al., 2013). Here, the present study aims to examine (1) the PM_{10} emission
119 potential of several typical landform types; (2) the seasonal variability of PM_{10}
120 emission; and (3) the implications for using PI-SWERL experimental data to
121 characterize the importance of specific landform types in contributing to
122 regional/global dust.

Methodology

Study area

The Tengger Desert and Mu Us Sandy Land, with an area of 45,800 km^2 and 39,000 km^2 respectively (Figure 1), are important dust sources in China (Wang et al., 2004; Zhang et al., 2003). A high frequency of dust storms has been reported from nearby meteorological stations during the period from 1981 to 2010, reaching up to 18 days year^{-1} in Minqin (Figure 1b). Strong winds (>17 m s^{-1}) occur frequently in spring and early summer amounting to between 4 and 40 days each year. The mean annual precipitation (MAP) ranges from 100 to 210 mm in the Tengger Desert and 260 to 420 mm in the Mu Us Sandy Land, mainly falling in summer (CMDC, 2012). Many landform types and distinct geomorphological units coexist in these two deserts (Figure 1). The Tengger Desert is dominated by mobile dunes (with vegetation cover less than 5%), while many parts of the Mu Us Sandy Land have been fixed or semi-fixed by vegetation in response to varying climate conditions (Mason et al., 2008; Xu et al., 2015).

Figure 1. Geomorphological settings of northern China (a) and study area (b). The upper map is extracted from the Land Use Map of China (RESDC, 2015) to show the spatial distribution of deserts (Wang Y et al., 2005). Descriptions of the land use classification system are detailed in Table S1. The boundaries of the Tengger Desert and Mu Us Sandy Land are derived from Zhu et al. (2013).

The numbers indicate major deserts and sandy lands: 1-Taklimakan, 2-Gurbantunggut, 3-Kumutage, 4-Gonghe, 5-Badain Jaran, 6-Tengger (the study area), 7-Ulan Buh, 8-Hobq, 9-Mu Us (the study area), 10-Otindag, 11-Horqin, 12-Songnen, 13-Hulunbeier.

Potential dust emissions were measured using the PI-SWERL at 341 sites (771 individual measurements) across the study area during April-May (spring, hereinafter AM), July-August (summer, hereinafter JA), October-early November (autumn, hereinafter ON) and late November-December (winter, hereinafter ND) between 2015 and 2016 (Table 1 and Figure 2). It is important to point out that while the repeat tests were not always carried out at precisely the same location in different seasons, the soil textural and surface characteristics of the tested landform types at each site were the same, hence the data obtained during different seasons can be appropriately compared. The selected sites included several typical landform types in the desert area including sparse grasslands, coppice dunes, sand dunes, interdunes, wadis, dry lake beds, stone pavements and dense grasslands (Figure 3). As it is recognized that wind erosion is reasonably effectively inhibited with vegetation cover above ~15-20% (e.g. Wiggs et al., 1995; Lancaster and Bass, 1998; Kimura et al. 2009), moderate grasslands were not differentiated from dense grasslands (Table 1). Surface sediment samples (the top 2-3 cm of the soil layer) were collected for standard analysis of gravimetric water content and particle size analysis with a Malvern Mastersizer 2000 (with a resolution of 0.02 to 2000 μm) using the treatment method proposed by Lu and An (1998). Each sample was pretreated with hydrogen peroxide (H_2O_2) and hydrochloric acid (HCl) to remove organic matter and carbonates. After over-night standing, samples were further dispersed with sodium metaphosphotate ($(NaPO3)_6$) under ultrasonic treatment for 10 minutes prior to analysis with the Mastersizer 2000. In addition, the soil textural properties of test sites were analyzed using the classification system of the United States Department of Agriculture (USDA) , based on the percentage contents of clay (<2 μm), silt (2-50 μm) and sand (50-2000 μm) (See the XLS file in supplementary material).

Figure 2. Location of test sites. Image of the study area is obtained from Google Earth (http://earth.google.com/). More information on the test sites is presented in the XLS file in the supplementary material.

Figure 3. Landform types and surface crusts tested with the PI-SWERL. Types: (a) sparse grassland, (b) coppice dune >2 m height, (c) coppice dune < 2 m height, (d) dune, (e) wadi, (f) dry lake, (g) stone pavement, and (h) dense grassland. Crust: (i) ephemeral crust, (j) silt-clay crust with cracks, (k) salt crust, and (l) biological crust.

PI-SWERL measurements

A miniature version of the PI-SWERL was used in the present study, which has been described in detail in Etyemezian et al. (2014). Briefly, the miniature PI-SWERL is an enclosed cylindrical chamber (D=30 cm, H=20 cm) that generates variable shear stresses on the ground surface using a rotating annular blade in close proximity to the surface. The PM_{10} concentration is measured by a nephelometer (DustTrak II model 8530) using a light scattering technique (Etyemezian et al., 2007; Sweeney et al., 2008) and sand movement is detected by optical gate sensors (OGS) mounted on the side of the chamber (Etyemezian et al., 2014). The OGS value (<7 counts per second) is regarded as background noise, indicating little to no saltation. A 20 s moving average of OGS values was used to minimize noise of the saltation data (Sweeney and Mason, 2013). Given potential damage caused to the instrument by vegetation (with height greater than 7 cm), the PI-SWERL was placed within bare patches for coppice dunes. For surfaces covered with short grass (< 3 cm) and gravel, the PI-SWERL was directly placed atop these elements.

At each site a ramp test, where the revolutions per minute (RPM) is linearly increased to simulate the effects of increasing wind, was first conducted to detect the threshold friction velocity (u_{*t}) for PM_{10} emission. The threshold was determined as the point at which the PM_{10} concentration began to increase consistently (similar in manner to the identification of a saltation threshold by Roney and White, 2004). The value of u_{*t} was calculated from the recorded RPM of the PI-SWERL using an equation based on surface properties:

$$U_{*eff}(RPM) = C_1 \times \alpha^4 \times RPM^{C_2/\alpha} \qquad (1)$$

Where C_1 and C_2 are constants and α is a calibration parameter based on surface roughness. The values of α applied in this study are presented in Table S2, as advised by Etyemezian et al. (2014) and Sweeney et al. (2016). The potential error in estimating u_{*t} associated with an incorrect selection of alpha (Δα=0.04) ranges from 7% to 20% for the typical threshold RPM range of 1000 to 3000. This is discussed in detail by Etyemezian et al. (2014).

Several hybrid tests were then performed, and each hybrid test consisted of three to four ramp tests and step tests. These step tests, where a target RPM was sustained for a given period before being increased to a new value, were used to measure the amount of emitted PM_{10} at specific values of u_* (Etyemezian et al., 2007). A total of three steps (with target RPMs of 2000, 3000 and 4000) were applied during each hybrid test. An additional RPM of 5000 was conducted for experiments in winter when surfaces were less erodible and on surfaces covered with roughness elements in any season. The emission flux during each step was calculated using the following equation proposed by Etyemezian et al. (2007):

$$E_i = \frac{\sum_{begin,i}^{end,i} (C \times F \times t_0)}{(t_{end,i} - t_{begin,i}) \times A_{eff}} \qquad (2)$$

Where C is the PM10 concentration (mg m^{-3}), F is the blower flow rate for fresh air (m^3 s^{-1}), A_{eff} is the effective area underneath the annular blade, with a constant value of 0.035 m^2 (Etyemezian et al., 2014), t is test time (s) at the beginning ($t_{begin,i}$) and ending ($t_{end,i}$) of each step level, i and t_0 is nephelometer sampling time.

Results

Characteristics of PM_{10} emission

As shown in Figure 4, PM_{10} concentration and saltation increased readily with increasing friction velocity (ramp tests, see light-colored segments), while their behaviors differed at test sites when the u_* was held constant (step tests, see dark-colored segments). According to differences in the temporal behavior of the data during the tests, PM_{10} emissions were categorized into four types:

(1) Sustained dust emission with strong saltation (Figure 4a). Saltation was active and sustained at high values of u_*. Where u_* remains constant, PM_{10} concentration is maintained at a relatively high level and is facilitated by consistently strong saltation.

(2) Moderate dust emission with decreasing saltation over time (Figure 4b). Similar to Type 1, but the difference was that PM_{10} concentrations reduced considerably following a peak in saltation at high and constant u_*. The reduction in saltation and PM_{10} concentrations were likely related to variations in soil strength or moisture that limited the availability of loose erodible material

after an initial period of strong erosion.

(3) Intermittent dust emission with little to no saltation (Figure 4c). In this case, saltation was of low intensity and sporadic. PM_{10} concentration rapidly decayed to the background level at a constant u_*. We interpret this as resulting from intermittent erosion by aerodynamic lift on supply-limited surfaces (Macpherson et al., 2008).

(4) Enhanced dust emission with moderate or strong saltation (Figure 4d). This type was common over disturbed surfaces. In contrast to Type 3, PM_{10} concentration increased markedly and maintained a high level at high u_* after disturbance. Here, dust emissions may originate from both aerodynamic lift and saltation since the availability of fine particles has been augmented by disturbance (Macpherson et al., 2008).

Figure 4. Four types of emission characteristics during PI-SWERL tests: (a) sustained dust emission with strong saltation; (b) moderate dust emission with decreasing saltation over time; (c) intermittent dust emission with little to no saltation; and (d) enhanced dust emission with moderate or strong saltation. Note that the OGS saltation and PM_{10} concentration axis on the right hand side in (c) is on a different scale. The pink lines are OGS saltation. The light red (blue) lines denote the changes of PM_{10} concentration (saltation, a 20 s moving average) at ramp tests. The dark red and blue lines represent their behaviors at step tests.

Analysis was undertaken to relate the measured emission characteristics with landform types and to explore how emission characteristics changed at a seasonal scale (Table 2). PM_{10} emissions from sparse grasslands, coppice dunes, interdunes, and dunes were mainly categorized as Type 1 emissions, although Type 2 emissions were evident on these landform types during ON (autumn) and ND (winter), especially for coppice dunes and interdunes. By contrast, Type 1 and Type 3 emissions were commonly found in wadis during all seasons, depending on the presence/absence of gravel and crust. Dry lake beds, stone pavements and dense grasslands were characterized by intermittent and low emissions in all seasons (Type 3 emissions). However, once these surfaces were disturbed, the emission potential was greatly enhanced (Type 1 and Type 4 emissions) in particular during AM (spring). The impact of disturbance appeared to be less significant in other seasons.

Seasonal variabilities of erosion thresholds and emission fluxes

Figure 5 illustrates the seasonal variations in erosion thresholds and PM_{10} fluxes of different landform types. In AM (spring), the geometric mean values of u_{*t} were relatively low over sparse grasslands, coppice dunes, interdunes, dunes and wadis, ranging from 0.30 to 0.40 m s^{-1}. By contrast, the threshold values were much larger over dry lake beds, stone pavements (~0.60 m s^{-1}), and dense grasslands (~0.50 m s^{-1}) due to the presence of crust and roughness elements (e.g. vegetation and gravel). However, once disturbed, the value of u_{*t} decreased by up to 54%. A substantial increase of up to 49% in the threshold values for PM_{10} emission was found during JA (summer). Erosion thresholds generally exhibited a second nadir for most landform types during ON (autumn), except for dry lake beds and dense grasslands due to their high moisture content (2.7% ±2.5% and 9.3% ± 4.3% respectively). In ND (winter), the increases in erosion thresholds were more pronounced, especially for dry lake beds, stone pavements and dense grasslands (by up to 170%). Even disturbed, the threshold values for PM_{10} emissions on dry lake beds, stone pavements and dense grasslands were still high and almost double that of AM (spring), probably resulting from the exposure of underlying moist soils after disturbance. In general, u_{*t} was low in spring and relatively high in winter. The different landform types can be ranked in descending order of u_{*t}: (1) stone pavements and dense grasslands (geometric mean: ~0.72 m s^{-1}); (2) dry lake beds (~0.66 m s^{-1}); (3) sparse grasslands, coppice dunes, interdunes and dunes (~0.38-0.42 m s^{-1}); (4) disturbed surfaces (0.31 m s^{-1}). This ranking is consistent with that of Gillette et al. (1980) (i.e. disturbed surfaces < sand dunes < dry lake beds < stone pavements). Moreover, our data suggest that seasonal variations in u_{*t} appeared to be more pronounced for dry lake beds, stone pavements, and dense grasslands.

In addition to u_{*t}, seasonal variability was also found in the PM_{10} emission flux (Figure 5), with similar trends evident at different values of applied u_* (Figure S1). PM_{10} emission fluxes were seen to generally be highest in AM (spring) and lowest in ND (winter) for most landform types except for wadis. While no clear seasonal trend was observed for wadi sites, PM_{10} emission was the lowest in JA (summer), which was probably due to the protective effects of surface crusting and soil aggregation (Figure 3i). For most landform types, the emission fluxes substantially decreased in JA (summer) and ON (autumn). For example, the PM_{10} fluxes emitted from sparse grasslands declined by about 80% and 60% in JA and ON respectively, with marked declines also evident for dry lake beds (by around 95%). In ND (winter), the decreases in emission fluxes were more considerable, within the range of 87% to 98%. As expected, PM_{10} emission fluxes were negatively correlated with u_{*t} (Figure S2 and Table 3). Also noticeable from Figure 5 is that PM_{10} emissions from disturbed surfaces, sparse grasslands, and coppice dunes were relatively high, with a range of 10^{-1} to 10^{1} mg m^{-2} s^{-1}. These values were up to five times the amount emitted from wadis, dunes and interdunes (~10^{-1}-10^{0} mg m^{-2} s^{-1}), and 1-2 orders of magnitude greater than dry lake beds, stone pavements and dense grasslands (~10^{-2} to 10^{-1} mg m^{-2} s^{-1}).

Figure 5. Geometric means and standard deviations of erosion thresholds and PM_{10} emission fluxes at u_*= 0.55 m s^{-1} from different landform types during April-May (AM), July-August (JA), October-early November (ON) and late November-December (ND). DS-disturbed surfaces, SG-sparse grassland, CD-coppice dune, ID-interdune, D-dune, W-wadi, DL-dry lake, SP-stone

pavement, DG-dense grassland.

Seasonal variations in soil moisture

Figure 6a shows the temporal changes in soil moisture content for the landform types. Overall, soil moisture contents were low in AM (spring) and JA (summer), and increased substantially in ON (autumn) and ND (winter). The general trend in soil moisture was in accord with the ratio of precipitation to evapotranspiration during test periods (Figure S3), which was derived from the monthly high-resolution (0.5°×0.5°) gridded dataset produced by the Climatic Research Unit (Harris et al., 2014). From the geomorphic perspective, moisture contents of dense grasslands and dry lake beds exhibited pronounced seasonal variations; whereas the moisture content values of other landform types were within a fairly narrow range across the four seasons. For example, the geometric mean moisture content of dense grasslands increased from 0.33% in AM (spring) to 7.5% and 11.8% in ON (autumn) and ND (winter) respectively. These values were around five times those of dry lake beds, and ten to fifty times greater than the moisture contents of other landform types. The high moisture contents of dense grasslands and dry lake beds may be related to the fine-textured soils (Table S3) and hygroscopic clay/saline minerals, which were able to absorb and retain water following precipitation (e.g. Williams et al., 1983; Pan and Wang, 2009).

Figure 6. Temporal variabilities in (a) soil moisture and (b) the relationship with PM_{10} flux at u_*= 0.55 m s^{-1} for different landform types. SG-sparse grassland; CD-coppice dune; ID-Interdune; D-dune; W-wadi; DL-dry lake; SP-stone pavement; DG-dense grassland. Features in b denote experimental data obtained from different landform types (by symbol shape) in different test periods (by symbol color, with the same legend in a). The inset in (b) shows data with gravimetric water content less than 1% (the left part of the dashed line).

Discussion

Moisture effects on PM_{10} emission

A negative relationship was found between PM_{10} flux and soil moisture content (Figure 6b). It seems that no significant emissions occurred when gravimetric moisture content exceeded 1%. This value is slightly lower than the proposed threshold value for dust suppression by previous studies, which ranges from 2% to 7% (Funk et al., 2008; Madden et al., 2010; Abulaiti et al., 2014; Munkhtsetseg et al., 2016).

Soil moisture characteristics show a strong relationship with landform type (Figure 6a) being controlled by the intrinsic soil properties such as soil texture, mineral composition and organic matter content (e.g. Williams et al., 1983; Zobeck, 1991). To explore the effect of moisture on the seasonality of PM_{10} emission, we analyzed the correlations between u*t, PM_{10} fluxes and soil moisture across all sites and seasons grouped by landform type (Table 3).

Overall, u_{*t} was positively correlated with soil moisture content, while PM_{10} flux was negatively correlated with moisture content. This finding is in accord with the concept of increasing moisture content enhancing the interparticle cohesion and efficiently inhibiting wind erosion (e.g. Chepil, 1956; Mckenna-Neuman and Nickling, 1989). Specifically, PM_{10} fluxes from dense grasslands, dry lake beds and stone pavements showed statistically strong negative correlations with moisture content (Table 3). Significant, albeit moderate, negative correlations were also found for coppice dunes and dunes.

Besides soil moisture, vegetation change, soil aggregation and surface crusting can also exert strong effects on dust emission by controlling the availability of loose erodible material at the monthly and seasonal scales (e.g. Zobeck, 1991; Webb and Strong, 2011). Since most of our sites were sparsely vegetated or vegetation-free, changing vegetation cover was unlikely to be the main factor responsible for the seasonality of PM_{10} emission. Moreover, it has long been recognized that moisture availability (e.g. alternating wetting and drying, freeze-thaw cycles) plays an important role in modulating aggregate stability and crust dynamics (e.g. Amézketa, 1999; Oztas and Fayetorbay, 2003; Nield et al., 2016). We therefore suggest that soil moisture was likely the primary factor controlling dust emission at our test sites over a seasonal scale. Attempts to better represent soil moisture and moisture-related effects on sediment supply availability may therefore be a key and worthwhile endeavor in improving large-scale simulations of dust cycle (Darmenova et al., 2009;

Haustein et al., 2015; Klose et al., 2019).

Landform type and dust emission potential

Characterization of the relative emissivity of different landform types is an important step forward for regional/global erodibility mapping and prescribing dust sources in regional/global models (Bullard et al., 2011; Parajuli and Zender, 2017). Owing to its small size and portability, the PI-SWERL offers great advantages in measuring small-scale variability in dust emission (Sweeney et al., 2011, von Holdt et al, 2019). Our results demonstrate the spatial and temporal heterogeneity in the characteristics and potential of PM_{10} emission (Figure 4 and Figure 5). Variations in emissions between and within landform types likely result from changes in the availability of loose erodible material, which is sensitive to soil texture, moisture content and roughness elements (Bullard et al., 2011; Webb and Strong, 2011). For example, sparse grasslands and coppice dunes have relatively high proportions of clay and silt (~2.8%-4.2%), and thereby produce sustained and high-magnitude emissions facilitated by strong saltation (Figure 4a). In contrast, sand dunes are unlikely to be high emitters of PM_{10} because they generally lack fine particles (mostly less than 2% in our study). However, it should be noted that a significant proportion of fines can be generated in dune systems by removal of iron oxides and clay coatings from the surfaces of sand grains during continuous saltation (e.g. Bullard et al., 2004; Bullard and White, 2005; Swet et al., 2019).

Finer-textured stone pavements and dense grasslands are characterized by emissions that attenuate over time (Figure 4c), as the sediment availability is limited due to soil aggregation and the sheltering effects of gravel and vegetation. The formation of surface crusts effectively reduces the emission potential of dry lake beds. Consequently, these surfaces are likely intermittent and low-magnitude emitters unless the supply limitation is alleviated by mechanical disturbances to the protective crusts. Additionally, seasonal variations in emissions appear to be more pronounced for these supply-limited surfaces, which may be related to large changes in moisture content (Figure 6).

Taking into account the measured PM_{10} emissions at specific friction velocities as applied by the PI-SWERL, the different tested landform types can be ranked by their propensity for emission : (1) disturbed surfaces; (2) sparse grasslands and coppice dunes; (3) wadis; (4) interdunes and dunes; (5) dry lake beds, stone pavements and dense grasslands. This ranking is consistent with PM_{10} emission rates measured by passive sand traps on specific landforms in other regions of China (coppice dunes > dunes > stony surfaces > grasslands; Wang et al., 2015) and in wind tunnel experiments (wadis/river beds > lakebeds > gobi; Wang et al., 2017).

Quantitative comparisons were made by linking the results presented here with our earlier study in July-August 2013 (Cui et al., 2015; Sweeney et al., 2016) and with other PI-SWERL experiments in the Mojave Desert in summer months (Sweeney et al., 2011) and in the Salton Sea (Sweeney et al., 2008, 2011; King et al., 2011). All these emissions were measured at the same friction velocity (u_*=0.55 m s^{-1}) and on a variety of landform types. Figure 7 illustrates the heterogeneity of emissions between and within different desert regions. Note that emission fluxes for coppice dunes were separated from those of dunes in the Mojave Desert experiments, which had been displayed together in Sweeney et al. (2011). Large variations are commonly found within the emission fluxes of individual landform types, with a span of one to three orders of magnitude. Compared to our earlier study (Cui et al., 2015; Sweeney et al., 2016), the present study appears to have a wider range of emission fluxes, which may be due to seasonal heterogeneity in PM_{10} emission that was not investigated in the earlier work. Coppice dunes and dunes exhibited a wide span of emission fluxes in our studies, and the highest emissions were around one order of magnitude greater than those measured in the Mojave Desert (Sweeney et al., 2011). The PM_{10} emissions from wadis in our work show agreement with those in the Salton Sea and emission fluxes from alluvial fans in the Mojave Desert. However, the highest emissions from those surfaces are one order of magnitude less than the value from dry ephemeral washes in the Mojave Desert. In contrast with the other two regions, emission fluxes measured from dry lake beds in our studies are within a fairly narrow range. This may be a consequence of the protection afforded by surface crusts against wind erosion, and/or an artifact of the relatively limited number of replicate tests on dry lake sites in our work. In general, coppice dunes and wadis are shown to be large emitters in both regions, while stone pavements are less emissive. Emissions from dry lake beds are highly variable and sensitive to crust type and strength, sand supply and groundwater level (e.g. Cahill et al., 1996; Reynolds et al., 2007; Sweeney et al., 2011). In comparison to previously measured data, our results demonstrate the importance of field data collected over a wide temporal range, which can provide insights into the seasonal and annual erodibility dynamics in potential dust source regions.

Figure 7. Box plot comparing PM_{10} fluxes from different landform types measured in the present study with other published PI-SWERL data at u*=0.55 m s^{-1}. The whiskers and boxes, from top to bottom, denote the 90^{th}, 75^{th}, median, 25^{th} percentiles and 10^{th} percentiles. Top and bottom dots represent maximum and minimum values. The white triangles in boxes denote the geometric means. Landform types: CD-coppice dune, W-wadi, D-dune, DL-dry lake, SP-stone pavement. Mojave-fan denotes distal alluvial fan. Dry lake sites in the Mojave Desert and the Salton Sea are classified into subgroups based on crust types (e.g. silt-clay and salt) and location (i.e. margin). Published data are from the Mojave Desert (Macpherson et al., 2008; Sweeney et al., 2011) and the Salton Sea, USA (Sweeney et al., 2008, 2011; King et al., 2011) as well as our prior study in China (Cui et al., 2015; Sweeney et al., 2016).

The identified emission potentials of landform types in this work broadly concur with the preferential dust source (PDS) scheme proposed by Bullard et al. (2011), which highlights the importance of sediment availability in controlling dust emission. Our measured data presented here, quantifying the seasonality of emissions, could provide information for characterizing the temporal behavior of identified preferential sources in this conceptual scheme. To develop our data further, we also compared our results to the sediment supply map (SSM) and land surface map (LSM) proposed by Parajuli and Zender (2017). The SSM values and LSM categories were extracted from the raster files based on the coordinates of our test sites. According to the LSM, a large proportion of sites were classified as stabilized sand deposits, bedrock and bedrock with sediment, which appeared to contradict our field observations (Figure S4). As demonstrated by Parajuli and Zender (2017), some inherent errors exist in the LSM classification, which might introduce errors in the interpretation of erodibility for specific surface types. The SSM was developed to represent global landscape-scale erodibility by integrating surface reflectance data into the geomorphic erodibility map of Zender et al. (2003b) (Parajuli and Zender, 2017). As suggested by Parajuli and Zender (2017), land surfaces that have high SSM values are considered as high emitting surfaces. However, no clear correlation was found between our measured fluxes and extracted SSM values (Figure 8). For instance, sparse grasslands and coppice dunes were identified as high emitters by the

PI-SWERL, but they were likely classified as low-emissive surfaces according to the SSM values (geometric means: ~0.19). In contrast, dry lake beds and stone pavements had relatively high SSM values (geometric means: ~0.26), but exhibited low emission potentials as evidenced from the PI-SWERL data. Similar disagreements between the SSM and observational data were also found in the Namib Desert by von Holdt et al. (2019). In this context, incorporation of field measurements is a clear priority in order to reliably represent the relationship between landform type and dust emission potential when using dust source schemes such as those of Parajuli and Zender (2017) and Bullard et al. (2011).

Figure 8. Box plot comparing measured PM_{10} fluxes at u_{*}= 0.55 m s^{-1} from different landform types across all seasons and corresponding values from the sediment supply map (SSM) of Parajuli and Zender (2017). The whiskers and boxes, from top to bottom, denote the 95th, 75th, median, 25th percentiles and 5th percentiles. Top and bottom dots/triangles represent the maximum and minimum values. The white circles with dots in boxes denote the geometric means. Landform types: SG-sparse grassland, CD-coppice dune, ID-interdune, D-dune, W-Wadi, DL-dry lake, SP-stone pavement, DG-dense grassland.

Conclusion

A better representation of dust sources is critical to quantifying the dust cycle and its impacts on climate and the environment. In this study, the PI-SWERL was used to investigate the emission potential of different landform types in northern China, and to examine the relationship between geomorphology and dust emission over a seasonal cycle.

For most landform types, PM_{10} emissions were the highest in spring, and the lowest in winter. Sparse grasslands and coppice dunes were large emitters in all seasons, whereas dry lake beds, stone pavements and dense grasslands were characterized by low-magnitude emissions. Moreover, seasonal variations in erosion thresholds and emission potentials were more pronounced on dry lake beds, stone pavements and dense grasslands. This is likely due to the greater dynamic changes in soil moisture content that effectively limit the supply of sediment available for erosion.

Comparisons with the PDS and SSM schemes demonstrate the importance of field measurements in capturing the spatial and temporal heterogeneity in dust emissions from different landform types. High-quality field data are useful in characterizing the erodibility of dust source regions and in constraining or validating dust models. Since the PI-SWERL is not directly related to natural wind conditions and unlikely to account for significant vegetation effects, additional data regarding aerodynamic roughness length, plant morphology and geometry are needed to build a more robust field dataset.

Acknowledgements

This work is supported by the National Key Research and Development Program of China (grant nos. 2016YFA0600503 and 2016YFE0109500), the National Natural Science Foundation of China (grant nos. 41690111). We wish to thank Professor James King (Université de Montréal, Canada) for providing the PI-SWERL results in Salton Sea; thank Dr. Sagar Parajuli (King Abdullah University of Science and Technology, Saudi Arabia) for providing raster files of global sediment supply map; thank Dr. Wancang Zhao and Dr. Xin Jia for their helpful suggestions on the paper. We gladly thank Jiang Wu, Yang Yu, Chenghong Liang, Yao Gu, Xi Chang, Jia Wan and Yu Ding, for their support during the PI-SWERL experiments in the field.

References

Abulaiti A, Kimura R, Shinoda M, Kurosaki Y, Mikami M, Ishizuka M, Yamada Y, Nishihara E and Gantsetseg B. 2014. An observational study of saltation and dust emission in a hotspot of Mongolia. Aeolian Research 15: 169-176. DOI: 10.1016/j.aeolia.2014.05.002

Albani S, Mahowald NM, Perry AT, Scanza RA, Zender CS, Heavens NG, Maggi V, Kok JF and Otto-Bliesner BL. 2014. Improved dust representation in the Community Atmosphere Model. Journal of Advances in Modeling Earth Systems 6(3): 541-570. DOI: 10.1002/2013MS000279

Amézketa E. 1999. Soil aggregate stability: A review. Journal of Sustainable Agriculture 14(2-3): 83-151. DOI: 10.1300/J064v14n02_08

Ashpole I and Washington R. 2013. A new high-resolution central and western Saharan summertime dust source map from automated satellite dust plume tracking. Journal of Geophysical Research: Atmospheres 118(13): 6981-6995. DOI: 10.1002/jgrd.50554

Baddock MC, Bullard JE and Bryant RG. 2009. Dust source identification using MODIS: A comparison of techniques applied to the Lake Eyre Basin, Australia. Remote Sensing of Environment 113(7): 1511-1528. DOI: 10.1016/j.rse.2009.03.002

Baddock MC, Ginoux P, Bullard JE and Gill TE. 2016. Do MODIS‐defined dust sources have a geomorphological signature? Geophysical Research Letters 43(6): 2606-2613. DOI: 10.1002/2015GL067327

Bielders CL, Rajot J and Amadou M. 2002. Transport of soil and nutrients by wind in bush fallow land and traditionally managed cultivated fields in the Sahel. Geoderma 109(1): 19-39. DOI: 10.1016/S0016-7061(02)00138-6

Brindley H, Knippertz P, Ryder C and Ashpole I. 2012. A critical evaluation of the ability of the Spinning Enhanced Visible and Infrared Imager (SEVIRI) thermal infrared red-green-blue rendering to identify dust events: Theoretical analysis. Journal of Geophysical Research: Atmospheres 117(D7). DOI: 10.1029/2011JD017326

Bullard JE, McTainsh GH and Pudmenzky C. 2004. Aeolian abrasion and modes of fine particle production from natural red dune sands: an experimental study. Sedimentology 51(5): 1103-1125. DOI: 10.1111/j.1365-3091.2004.00662.x

Bullard JE and White K. 2005. Dust production and the release of iron oxides resulting from the aeolian abrasion of natural dune sands. Earth Surface Processes and Landforms 30(1): 95-106. DOI: 10.1002/esp.1148

Bullard J. 2010. Bridging the gap between field data and global models: Current strategies in aeolian research. Earth Surface Processes and Landforms. DOI: 10.1002/esp.1958

Bullard JE, Harrison SP, Baddock MC, Drake N, Gill TE, McTainsh G and Sun Y. 2011. Preferential dust sources: A geomorphological classification designed for use in global dust-cycle models. Journal of Geophysical Research: Earth Surface 116: F04034. DOI: 10.1029/2011JF002061

Cahill TA, Gill TE, Reid JS, Gearhart EA and Gillette DA. 1996. Saltating particles, playa crusts and dust aerosols at Owens (dry) Lake, California. Earth Surface Processes and Landforms 21(7): 621-639. DOI: 10.1002/(SICI)1096-9837(199607)21:7<621::AID-ESP661>3.0.CO;2-E

Cakmur RV, Miller RL, Perlwitz J, Geogdzhayev IV, Ginoux P, Koch D, Kohfeld KE, Tegen I and Zender CS. 2006. Constraining the magnitude of the global dust cycle by minimizing the difference between a model and observations. Journal of Geophysical Research 111(D6). DOI: 10.1029/2005JD005791

Chepil W. 1956. Influence of moisture on erodibility of soil by wind. Soil Science Society of America Journal 20(2): 288-292. DOI: 10.2136/sssaj1956.03615995002000020033x

China Meteorological Data Service Center (CMDC), 2012. Dataset Of Daily Surface Observation Values In Individual Years (1981-2010) In China (available at http://data.cma.cn/).

Cui M, Lu H, Sweeney MR, Mason JA, Feng H and Xu Z. 2015. PM10 emission flux in the Tengger Desert and Mu Us Sand field, northern China, measured by PI-SWERL. Science Bulletin 60(17): 1621-1630. DOI:10.1360/N972014-01157

Darmenova K, Sokolik IN, Shao Y, Marticorena B and Bergametti G. 2009. Development of a physically based dust emission module within the Weather Research and Forecasting (WRF) model: Assessment of dust emission parameterizations and input parameters for source regions in Central and East Asia. Journal of Geophysical Research 114: D14201. DOI: 10.1029/2008JD011236

Etyemezian V, Nikolich G, Ahonen S, Pitchford M, Sweeney M, Purcell R, Gillies J and Kuhns H. 2007. The Portable In Situ Wind Erosion Laboratory (PI-SWERL): A new method to measure PM 10 windblown dust properties and potential for emissions. Atmospheric Environment 41(18): 3789-3796. DOI: 10.1016/j.atmosenv.2007.01.018

Etyemezian V, Gillies JA, Shinoda M, Nikolich G, King J and Bardis AR. 2014. Accounting for surface roughness on measurements conducted with PI-SWERL: Evaluation of a subjective visual approach and a photogrammetric technique. Aeolian Research 13: 35-50. DOI: 10.1016/j.aeolia.2014.03.002

Evan AT, Vimont DJ, Heidinger AK, Kossin JP and Bennartz R. 2009. The role of aerosols in the evolution of tropical north atlantic ocean temperature anomalies. Science 324(5928): 778-781. DOI: 10.1126/science.1167404

Funk R, Reuter HI, Hoffmann C, Engel W and Öttl D. 2008. Effect of moisture on fine dust emission from tillage operations on agricultural soils. Earth Surface Processes and Landforms 33(12): 1851-1863. DOI: 10.1002/esp.1737

Ginoux P, Chin M, Tegen I, Prospero JM, Holben B, Dubovik O and Lin SJ. 2001. Sources and distributions of dust aerosols simulated with the

GOCART model. Journal of Geophysical Research: Atmospheres 106(D17): 20255 - 20273. DOI: 10.1029/2000JD000053

Ginoux P, Prospero JM, Gill TE, Hsu NC and Zhao M. 2012. Global-scale attribution of anthropogenic and natural dust sources and their emission rates based on MODIS Deep Blue aerosol products. Reviews of Geophysics 50(3). DOI: 10.1029/2012RG000388

Grini A, Myhre G, Zender CS and Isaksen ISA. 2005. Model simulations of dust sources and transport in the global atmosphere: Effects of soil erodibility and wind speed variability. Journal of Geophysical Research 110(D2). DOI: 10.1029/2004JD005037

Harris I, Jones PD, Osborn TJ and Lister DH. 2014. Updated high-resolution grids of monthly climatic observations – the CRU TS3.10 Dataset. International Journal of Climatology 34(3): 623-642. DOI: 10.1002/joc.3711

Haustein K, Washington R, King J, Wiggs G, Thomas DSG, Eckardt FD, Bryant RG and Menut L. 2015. Testing the performance of state-of-the-art dust emission schemes using DO4Models field data. Geoscientific Model Development 8(2): 341-362. DOI: 10.5194/gmd-8-341-2015

Huneeus N, Schulz M, Balkanski Y, Griesfeller J, Prospero J, Kinne S, Bauer S, Boucher O, Chin M, Dentener F, Diehl T, Easter R, Fillmore D, Ghan S, Ginoux P, Grini A, Horowitz L, Koch D, Krol MC, Landing W, Liu X, Mahowald N, Miller R, Morcrette JJ, Myhre G, Penner J, Perlwitz J, Stier P, 689 Takemura T and Zender CS. 2011. Global dust model intercomparison in AeroCom phase I. Atmospheric Chemistry and Physics 11(15): 7781-7816. DOI: 10.5194/acp-11-7781-2011

692 Jickells TD, An ZS, Andersen KK, Baker AR, Bergametti G, Brooks N, Cao JJ, Boyd PW, Duce RA, Hunter KA, Kawahata H, Kubilay N, LaRoche J, Liss PS, Mahowald N, Prospero JM, Ridgwell AJ, Tegen I and Torres R. 2005. Global iron connections between desert dust, ocean biogeochemistry, and climate. Science 308(5718): 67-71. DOI: 10.1126/science.1105959

697 Karydis VA, Tsimpidi AP, Bacer S, Pozzer A, Nenes A and Lelieveld J. 2017. Global impact of mineral dust on cloud droplet number concentration. Atmospheric Chemistry and Physics 17(9): 5601-5621. DOI: 10.5194/acp-17-5601-2017

701 Katra I, Gross A, Swet N, Tanner S, Krasnov H and Angert A. 2016. Substantial dust loss of bioavailable phosphorus from agricultural soils. Scientific Reports 6: 24736. DOI: 10.1038/srep24736

704 Kellogg CA and Griffin DW. 2006. Aerobiology and the global transport of desert dust. Trends in Ecology & Evolution 21(11): 638-644. DOI: 10.1016/j.tree.2006.07.004

707 King J, Etyemezian V, Sweeney M, Buck BJ and Nikolich G. 2011. Dust emission variability at the Salton Sea, California, USA. Aeolian Research 3(1): 67-79. DOI: 10.1016/j.aeolia.2011.03.005

710 Kimura RJ, Bai L and Wang JM. 2009. Relationships among dust outbreaks,

vegetation cover, and surface soil water content on the Loess Plateau of China, 1999–2000. CATENA 77(3): 292-296. DOI: 10.1016/j.catena.2009.02.016

Klose M, Gill TE, Etyemezian V, Nikolich G, Ghodsi Zadeh Z, Webb NP and Van Pelt RS. 2019. Dust emission from crusted surfaces: Insights from field measurements and modelling. Aeolian Research 40: 1-14. DOI: 10.1016/j.aeolia.2019.05.001

Kok JF, Albani S, Mahowald NM and Ward DS. 2014. An improved dust emission model – Part 2: Evaluation in the Community Earth System Model, with implications for the use of dust source functions. Atmospheric Chemistry and Physics 14(23): 13043-13061. DOI: 10.5194/acp-14-13043-2014

Kok JF, Ridley DA, Zhou Q, Miller RL, Zhao C, Heald CL, Ward DS, Albani S and Haustein K. 2017. Smaller desert dust cooling effect estimated from analysis of dust size and abundance. Nature Geoscience. DOI: 10.1038/ngeo2912

Kok JF, Ward DS, Mahowald NM and Evan AT. 2018. Global and regional importance of the direct dust-climate feedback. Nature Communications 9(1): 241. DOI: 10.1038/s41467-017-02620-y

Koven CD and Fung I. 2008. Identifying global dust source areas using high-resolution land surface form. Journal of Geophysical Research 113(D22). DOI: 10.1029/2008JD010195

Lancaster N and Baas A. 1998. Influence of vegetation cover on sand transport by wind: field studies at Owens Lake, California. Earth Surface Processes and Landforms 23(1): 69-82. DOI: 10.1002/(SICI)1096-9837(199801)23:13.0.CO;2-G

Lee JA, Baddock MC, Mbongowo JM and Thomas EG. 2012. Geomorphic and land cover characteristics of aeolian dust sources in West Texas and eastern New Mexico, USA. Aeolian Research 3: 459-466. DOI: 10.1016/j.aeolia.2011.08.001

Lu HY and An ZS. 1998. Pretreated methods on loess-palaeosol samples granulometry. Chinese Science Bulletin 43(3): 237-240. DOI: 10.1007/BF02898920

Lu H, Yi S, Xu Z, Zhou Y, Zeng L, Zhu F, Feng H, Dong L, Zhuo H, Yu K, Mason J, Wang X, Chen Y, Lu Q, Wu B, Dong Z, Qu J, Wang X and Guo Z. 2013. Chinese deserts and sand fields in Last Glacial Maximum and Holocene Optimum. Chinese Science Bulletin 58(23): 2775-2783. DOI: 10.1007/s11434-013-5919-7

Macpherson T, Nickling WG, Gillies JA and Etyemezian V. 2008. Dust emissions from undisturbed and disturbed supply-limited desert surfaces. Journal of Geophysical Research: Earth Surface 113(F2). DOI: 10.1029/2007JF000800

Madden NM, Southard RJ and Mitchell JP. 2010. Soil water and particle size distribution influence laboratory-generated PM10. Atmospheric

Environment 44(6): 745-752. DOI: 10.1016/j.atmosenv.2009.11.044

Mahowald N, Jickells TD, Baker AR, Artaxo P, Benitez-Nelson CR, Bergametti G, Bond TC, Chen Y, Cohen DD, Herut B, Kubilay N, Losno R, Luo C, Maenhaut W, McGee KA, Okin GS, Siefert RL and Tsukuda S. 2008. Global distribution of atmospheric phosphorus sources, concentrations and deposition rates, and anthropogenic impacts. Global Biogeochemical Cycles 22(GB40264). DOI: 10.1029/2008GB003240

Mahowald NM, Muhs DR, Levis S, Rasch PJ, Yoshioka M, Zender CS and Luo C. 2006. Change in atmospheric mineral aerosols in response to climate: Last glacial period, preindustrial, modern, and doubled carbon dioxide climates. Journal of Geophysical Research: Atmospheres 111(D10). DOI: 10.1029/2005JD006653

Mahowald NM, Hamilton DS, Mackey KRM, Moore JK, Baker AR, Scanza RA and Zhang Y. 2018. Aerosol trace metal leaching and impacts on marine microorganisms. Nature Communications 9(1). DOI: 10.1038/s41467-018-04970-7

Mason JA, Swinehart JB, Lu H, Miao X, Cha P and Zhou Y. 2008. Limited change in dune mobility in response to a large decrease in wind power in semi-arid northern China since the 1970s. Geomorphology 102(3): 351-363. DOI: 10.1016/j.geomorph.2008.04.004

McKenna-Neuman C and Nickling WG. 1989. A theoretical and wind tunnel investigation of the effect of capillary water on the entrainment of sediment by wind. Canadian Journal of Soil Science 69(1): 79-96. DOI: 10.4141/cjss89-008

Middleton NJ. 2017. Desert dust hazards: A global review. Aeolian Research 24: 53-63. DOI: 10.1016/j.aeolia.2016.12.001

Munkhtsetseg E, Shinoda M, Gillies JA, Kimura R, King J and Nikolich G. 2016. Relationships between soil moisture and dust emissions in a bare sandy soil of Mongolia. Particuology 28: 131-137. DOI: 10.1016/j.partic.2016.03.001

Munkhtsetseg E, Shinoda M, Ishizuka M, Mikami M, Kimura R and Nikolich G. 2017. Anthropogenic dust emissions due to livestock trampling in a Mongolian temperate grassland. Atmospheric Chemistry and Physics 17(18): 11389-11401. DOI: 10.5194/acp-17-11389-2017

Nield JM, Wiggs GFS, King J, Bryant RG, Eckardt FD, Thomas DSG and Washington R. 2016. Climate-surface-pore-water interactions on a salt crusted playa: Implications for crust pattern and surface roughness development measured using terrestrial laser scanning. Earth Surface Processes and Landforms 41(6): 738-753. DOI: 10.1002/esp.3860

Okin GS, Mahowald N, Chadwick OA and Artaxo P. 2004. Impact of desert dust on the biogeochemistry of phosphorus in terrestrial ecosystems. Global Biogeochemical Cycles 18(2). DOI: 10.1029/2003GB002145

Oztas T and Fayetorbay F. 2003. Effect of freezing and thawing processes on soil aggregate stability. Catena 52(1): 1-8. DOI:

10.1016/S0341-8162(02)00177-7

Pan YX and Wang XP. 2009. Factors controlling the spatial variability of surface soil moisture within revegetated-stabilized desert ecosystems of the Tengger Desert, Northern China. Hydrological Processes 23(11): 1591-1601. DOI: 10.1002/hyp.7287

Parajuli SP, Yang Z and Kocurek G. 2014. Mapping erodibility in dust source regions based on geomorphology, meteorology, and remote sensing. Journal of Geophysical Research: Earth Surface 119(9): 1977-1994. DOI: 10.1002/2014JF003095

Parajuli SP and Zender CS. 2017. Connecting geomorphology to dust emission through high-resolution mapping of global land cover and sediment supply. Aeolian Research 27: 47-65. DOI: 10.1016/j.aeolia.2017.06.002

Resource and Environment Science Data Center, Chinese Academy of Sciences (RESDC), 2015. The Land Use Map of China in 2015 (available at http://www.resdc.cn/).

Reynolds RL, Yount JC, Reheis M, Goldstein H, Chavez P, Fulton R, Whitney J, Fuller C and Forester RM. 2007. Dust emission from wet and dry playas in the Mojave Desert, USA. Earth Surface Processes and Landforms 32(12): 1811-1827. DOI: 10.1002/esp.1515

Roney JA and White BR. 2004. Definition and measurement of dust aeolian thresholds. Journal of Geophysical Research: Earth Surface 109(F1). DOI:

10.1029/2003JF000061

Sankey JB, Eitel JUH, Glenn NF, Germino MJ and Vierling LA. 2011. Quantifying relationships of burning, roughness, and potential dust emission with laser altimetry of soil surfaces at submeter scales. Geomorphology 135(1-2): 181-190. DOI: 10.1016/j.geomorph.2011.08.016

Shao Y. 2008. Physics and modelling of wind erosion, 37. Springer Netherlands: Dordrecht

Shao Y, Wyrwoll K, Chappell A, Huang J, Lin Z, McTainsh GH, Mikami M, Tanaka TY, Wang X and Yoon S. 2011. Dust cycle: An emerging core theme in Earth system science. Aeolian Research 2(4): 181-204. DOI: 10.1016/j.aeolia.2011.02.001

Sweeney M, Etyemezian V, Macpherson T, Nickling W, Gillies J, Nikolich G and McDonald E. 2008. Comparison of PI-SWERL with dust emission measurements from a straight - line field wind tunnel. Journal of Geophysical Research: Earth Surface 113(F1). DOI: 10.1029/2007JF000830

Sweeney MR, McDonald EV and Etyemezian V. 2011. Quantifying dust emissions from desert landforms, eastern Mojave Desert, USA. Geomorphology 135(1): 21-34. DOI: 10.1016/j.geomorph.2011.07.022

Sweeney MR and Mason JA. 2013. Mechanisms of dust emission from Pleistocene loess deposits, Nebraska, USA. Journal of Geophysical

Research: Earth Surface 118(3): 1460-1471. DOI: 10.1002/jgrf.20101

Sweeney MR, Lu H, Cui M, Mason JA, Feng H and Xu Z. 2016. Sand dunes as potential sources of dust in northern China. Science China Earth Sciences 59(4): 760-769. DOI: 10.1007/s11430-015-5246-8

Swet N, Elperin T, Kok JF, Martin RL, Yizhaq H and Katra I. 2019. Can active sands generate dust particles by wind-induced processes? Earth and Planetary Science Letters 506: 371-380. DOI: 10.1016/j.epsl.2018.11.013

Tegen I, Lacis AA and Fung I. 1996. The influence on climate forcing of mineral aerosols from disturbed soils. Nature 380(6573): 419-422. DOI: 10.1038/380419a0

von Holdt JR, Eckardt FD and Wiggs GFS. 2017. Landsat identifies aeolian dust emission dynamics at the landform scale. Remote Sensing of Environment 198: 229-243. DOI: 10.1016/j.rse.2017.06.010

von Holdt JRC, Eckardt FD, Baddock MC and Wiggs GFS. 2019. Assessing landscape dust emission potential using combined ground - based measurements and remote sensing data. Journal of Geophysical Research: Earth Surface 124: 1080-1098. DOI: 10.1029/2018JF004713.

Wang H, Jia X, Li K and Li Y. 2015. Horizontal wind erosion flux and potential dust emission in arid and semiarid regions of China: A major source area for East Asia dust storms. Catena 133: 373-384. DOI: 10.1016/j.catena.2015.06.011

Wang XM, Dong ZB, Zhang JW and Liu LC. 2004. Modern dust storms in

China: an overview. Journal of Arid Environments 58(4): 559-574. DOI: 10.1016/j.jaridenv.2003.11.009

Wang X, Dong Z, Yan P, Yang Z and Hu Z. 2005. Surface sample collection and dust source analysis in northwestern China. CATENA 59(1): 35-53. DOI: 10.1016/j.catena.2004.05.009

Wang X, Chen F, Hasi E and Li J. 2008. Desertification in China: An assessment. Earth-Science Reviews 88(3–4): 188-206. DOI: 10.1016/j.earscirev.2008.02.001

Wang X, Cheng H, Che H, Sun J, Lu H, Qiang M, Hua T, Zhu B, Li H, Ma W, Lang L, Jiao L and Li D. 2017. Modern dust aerosol availability in northwestern China. Scientific Reports 7(1). DOI: 10.1038/s41598-017-09458-w

Wang Y, Wang J, Qi Y and Yan C. 2005. 1:100,000 scale desert distribution mapset of China (available at http://westdc.westgis.ac.cn).

Webb NP and McGowan HA. 2009. Approaches to modelling land erodibility by wind. Progress in Physical Geography 33(5): 587-613. DOI: 10.1177/0309133309341604

Webb NP and Strong CL. 2011. Soil erodibility dynamics and its representation for wind erosion and dust emission models. Aeolian Research 3(2): 165-179. DOI: 10.1016/j.aeolia.2011.03.002

Wiggs GFS, Thomas DSG, Bullard JE and Livingstone I. 1995. Dune mobility and vegetation cover in the Southwest Kalahari Desert. Earth Surface

887 Processes and Landforms 20: 515-529. DOI: 10.1002/esp.3290200604

888 Williams J, Prebble RE, Williams WT and Hignett CT. 1983. The influence of texture, structure and clay mineralogy on the soil moisture characteristic. Soil Research 21(1): 15-32. DOI: 10.1071/SR9830015

891 Wu C, Lin Z, He J, Zhang M, Liu X, Zhang R and Brown H. 2016. A process-oriented evaluation of dust emission parameterizations in CESM: Simulation of a typical severe dust storm in East Asia. Journal of Advances in Modeling Earth Systems 8(3): 1432-1452. DOI: 10.1002/2016MS000723

896 Xu Z, Mason JA and Lu H. 2015. Vegetated dune morphodynamics during recent stabilization of the Mu Us dune field, north-central China. Geomorphology 228: 486-503. DOI: 10.1016/j.geomorph.2014.10.001

899 Yin Y and Chen L. 2007. The effects of heating by transported dust layers on cloud and precipitation: A numerical study. Atmospheric Chemistry and Physics 7(13): 3497-3505. DOI: 10.5194/acp-7-3497-2007

902 Zender CS, Bian H and Newman D. 2003a. Mineral Dust Entrainment and Deposition (DEAD) model: Description and 1990s dust climatology. Journal of Geophysical Research: Atmospheres 108(D14). DOI: 10.1029/2002JD002775

906 Zender CS, Newman D and Torres O. 2003b. Spatial heterogeneity in aeolian erodibility: Uniform, topographic, geomorphic, and hydrologic hypotheses. Journal of Geophysical Research 108(D17): 4543. DOI:

10.1029/2002JD003039

Zender CS and Kwon EY. 2005. Regional contrasts in dust emission responses to climate. Journal of Geophysical Research-Atmospheres 110(D13201D13). DOI: 10.1029/2004JD005501

Zhang XY, Gong SL, Zhao TL, Arimoto R, Wang YQ and Zhou ZJ. 2003. Sources of Asian dust and role of climate change versus desertification in Asian dust emission. Geophysical Research Letters 30(24). DOI: 10.1029/2003GL018206

Zhu FY, Lu HY, Zhang WC, Chen YY, Zeng L, Xu ZW, Zhang HZ and Dong LN. 2013. Mapping Deserts and Sandy Fields in Northern China and Surface Process Analysis Based on 3S Techniques. Quaternary Sciences 33(2): 197-205. DOI: 10.3969/j.issn.1001-7410.2013.02.01

Zobeck TM. 1991. Soil properties affecting wind erosion. Journal of Soil and Water Conservation 46(2): 112 -118.

Table 1. Test locations.

Type[a]	Main characteristics	Number of sites (PI-SWERL tests)				
		Apr.-May. (spring)	Jul.-Aug. (summer)	Oct.-early Nov. (autumn)	Late Nov.-Dec. (winter)	total
Sparse grassland	Herbaceous canopy cover between 5% and 20%	13(28)	11 (23)	7 (19)	10 (23)	41 (93)
Coppice dune	Vegetated sand dunes	33 (67)	21 (42)	18 (47)	19 (38)	91 (194)
Interdune	Gently sloping areas between dunes, with vegetation cover less than 5%	10 (20)	9(18)	7 (20)	6 (12)	32 (70)
Dune	Sand dunes, no vegetation	23 (79)	16 (36)	25 (67)	22 (44)	86 (226)
Wadi	Relics of river channels	9 (18)	5 (12)	3 (8)	2 (4)	19 (42)

Dry lake	Flat-bottomed, often with salt crusts	3 (6)	3 (7)	5 (10)	2 (5)	13 (28)
Stone pavement	Low angle surfaces covered with gravel	3 (6)	6 (12)	3 (6)	2 (4)	14 (28)
Dense grassland[b]	Herbaceous canopy cover greater than 20%	6 (12)	2 (4)	4 (8)	6 (12)	18 (36)
Disturbed surface[c]	Disturbance exerted to surface roughness	8 (16)	8 (16)	7 (14)	4 (8)	27 (54)

[a]Modified after the classification system of the National Land Use Map (RESDC, 2015), as shown in the Table S1.

[b]Moderate grass (with canopy cover between 20% and 50%) and dense grass (with canopy cover greater than 50%) are categorized into dense grassland.

[c]Disturbance includes 1) breaking down salt crusts or spreading a layer of sand on top of silt-clay crusts for dry lake beds, 2) removal of gravel from stone pavements, 3) scraping the grass from moderate to dense grasslands.

Table 2. Number of test sites categorized by four types of emission characteristics.

	Apr.-May. (spring)				Jul.-Aug. (summer)				Oct.-early Nov. (autumn)				Late Nov.-Dec. (winter)[b]			
	Type 1	Type 2	Type 3	Type 4	Type 1	Type 2	Type 3	Type 4	Type 1	Type 2	Type 3	Type 4	Type 1	Type 2	Type 3	Type 4
SG	12		1[a]		11				7				7	3		
CD	29	4			18	3			11	7			8	10		
ID	9	1			7	1	1[a]		4	3			2	4		
D	20	3			14	2			14	11			13	8		
W	7		2		2		3		3				2			
DL	3				1		2		1		4					
SP			3				6				3					
DG			6				2				4				2	
DS	2			6	4	2	1	1	2	1	2	2		2	2	

[a]SG-sparse grassland, CD-coppice dune, ID-interdune, D-dune, W-wadi, DL-dry lake, SP-stone pavement, DG-dense grassland.

[b]The surface is partly with crust and/or soil aggregation.

[c]Some sites with PM_{10} fluxes less than 0.01 mg m^{-2} s^{-1} in Late Nov.-Dec. are not presented.

Table 3. Spearman rank correlation coefficients between erosion thresholds, emission fluxes and soil moisture for different landform types.

	wt% H_2O -u_{*t}	wt% H_2O -Flux1	wt% H_2O -Flux2	wt% H_2O -Flux3
Sparse grassland	0.139	-0.018	-0.055	-0.236
Coppice dune	0.236*	-0.237*	**-0.321****	**-0.392****
Interdune	0.195	-0.115	-0.172	-0.270
Dune	0.121	-0.148	**-0.353****	**-0.438****
Wadi	0.466	-0.037	-0.119	-0.286
Dry lake	0.478	**-0.725****	**-0.808****	**-0.753****
Stone pavement	0.171	-0.187	-0.473	-0.597*
Dense grassland	**0.726****	-0.376	-0.568*	**-0.807****

**Significance level (two-tailed test) below 0.01; * Significance level (two-tailed test) below 0.05.

[a]Flux1, Flux2 and Flux3 denote PM_{10} emission flux at u^*= 0.39, 0.55 and 0.69 respectively.

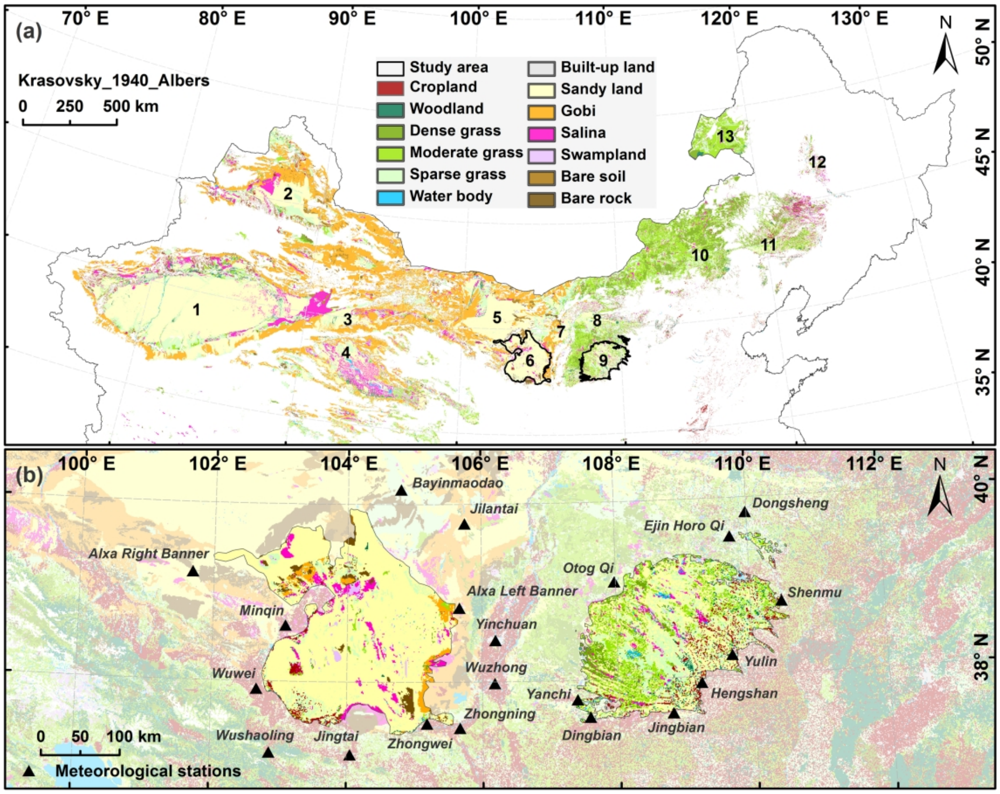

Figure 1. Geomorphological settings of northern China (a) and study area (b). The upper map is extracted from the Land Use Map of China (RESDC, 2015) to show the spatial distribution of deserts (Wang Y et al., 2005). Descriptions of the land use classification system are detailed in Table S1. The boundaries of the Tengger Desert and Mu Us Sandy Land are derived from Zhu et al. (2013). The numbers indicate major deserts and sandy lands: 1-Taklimakan, 2-Gurbantunggut, 3-Kumutage, 4-Gonghe, 5-Badain Jaran, 6-Tengger (the study area), 7-Ulan Buh, 8-Hobq, 9-Mu Us (the study area), 10-Otindag, 11-Horqin, 12-Songnen, 13-Hulunbeier.

254x201mm (300 x 300 DPI)

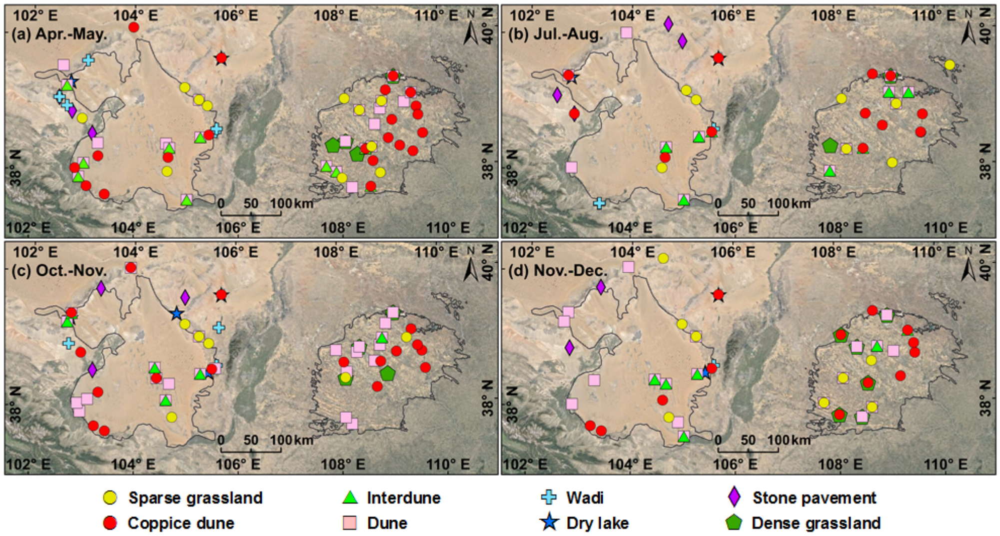

Figure 2. Location of test sites. Image of the study area is obtained from Google Earth (http://earth.google.com/). More information on the test sites is presented in the XLS file in the supplementary material.

261x141mm (96 x 96 DPI)

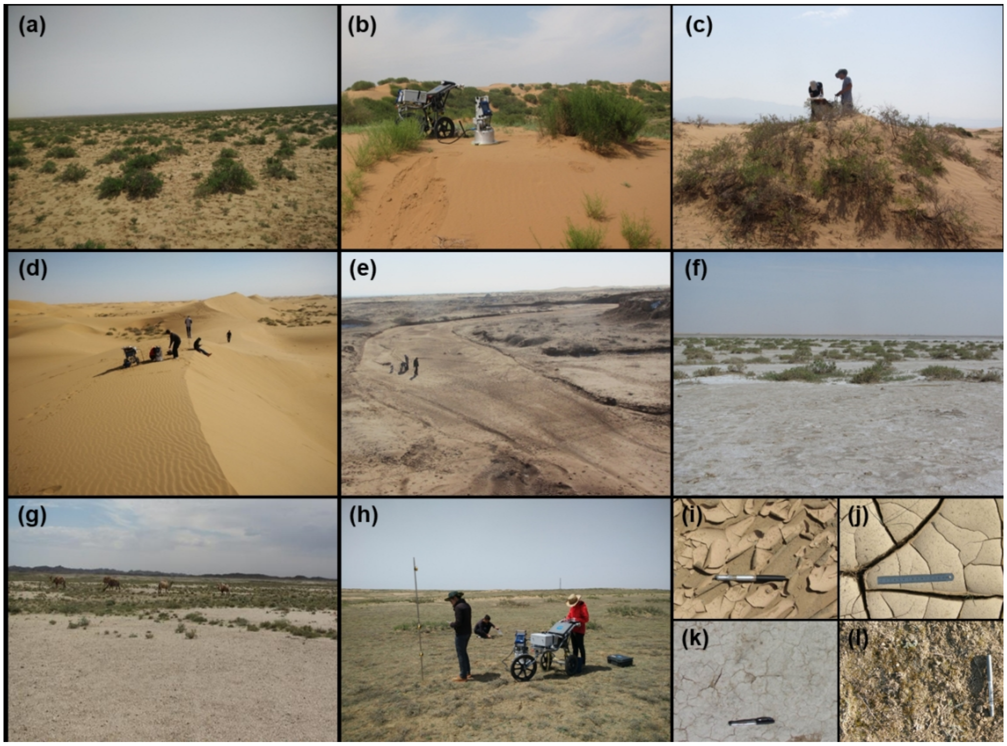

Figure 3. Landform types and surface crusts tested with the PI-SWERL. Types: (a) sparse grassland, (b) coppice dune >2 m height, (c) coppice dune < 2 m height, (d) dune, (e) wadi, (f) dry lake, (g) stone pavement, and (h) dense grassland. Crust: (i) ephemeral crust, (j) silt-clay crust with cracks, (k) salt crust, and (l) biological crust.

217x160mm (150 x 150 DPI)

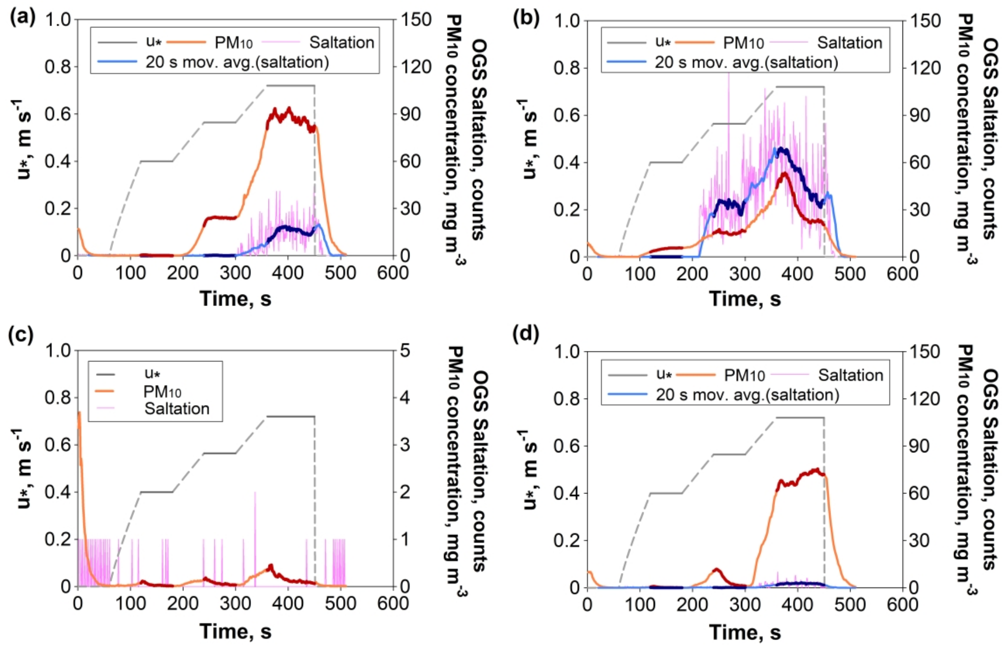

Figure 4. Four types of emission characteristics during PI-SWERL tests: (a) sustained dust emission with strong saltation; (b) moderate dust emission with decreasing saltation over time; (c) intermittent dust emission with little to no saltation; and (d) enhanced dust emission with moderate or strong saltation. Note that the OGS saltation and PM10 concentration axis on the right hand side in (c) is on a different scale. The pink lines are OGS saltation. The light red (blue) lines denote the changes of PM10 concentration (saltation, a 20 s moving average) at ramp tests. The dark red and blue lines represent their behaviors at step tests.

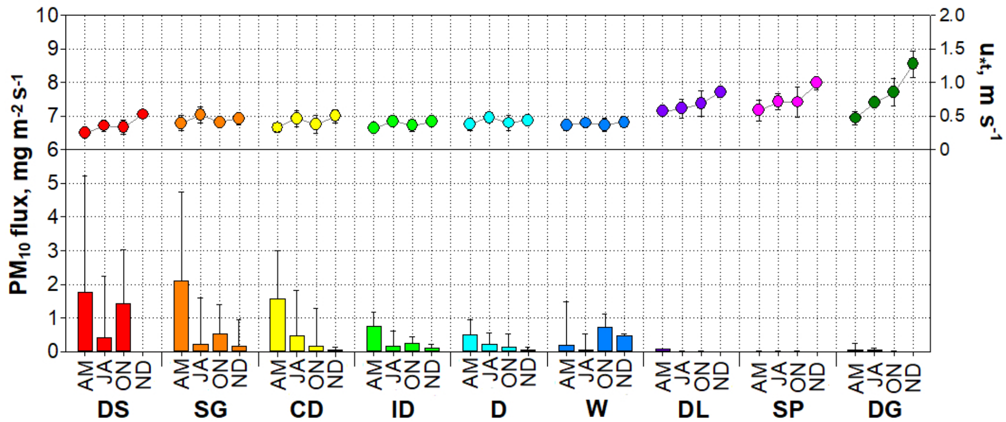

Figure 5. Geometric means and standard deviations of erosion thresholds and PM10 emission fluxes at u*= 0.55 m s-1 from different landform types during April-May (AM), July-August (JA), October-early November (ON) and late November-December (ND). DS-disturbed surfaces, SG-sparse grassland, CD-coppice dune, ID-interdune, D-dune, W-wadi, DL-dry lake, SP-stone pavement, DG-dense grassland.

278x117mm (96 x 96 DPI)

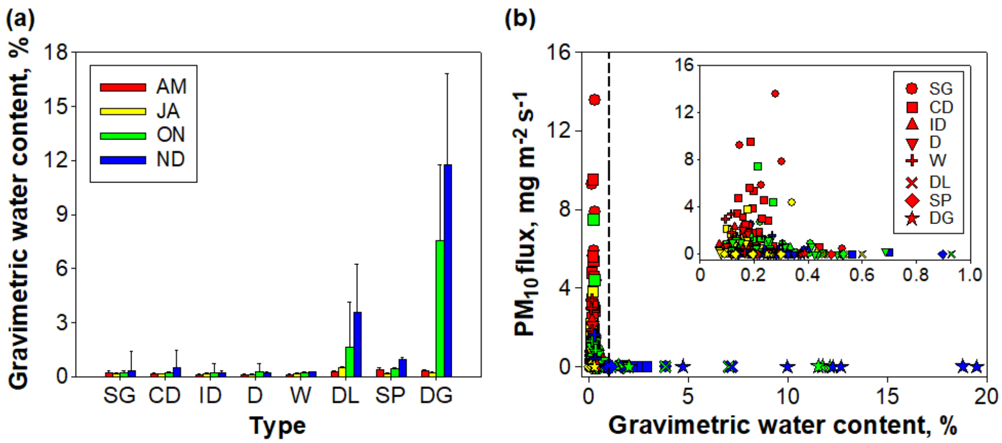

Figure 6. Temporal variabilities in (a) soil moisture and (b) the relationship with PM10 flux at u*= 0.55 m s-1 for different landform types. SG-sparse grassland; CD-coppice dune; ID-Interdune; D-dune; W-wadi; DL-dry lake; SP-stone pavement; DG-dense grassland. Features in b denote experimental data obtained from different landform types (by symbol shape) in different test periods (by symbol color, with the same legend in a). The inset in (b) shows data with gravimetric water content less than 1% (the left part of the dashed line).

257x112mm (96 x 96 DPI)

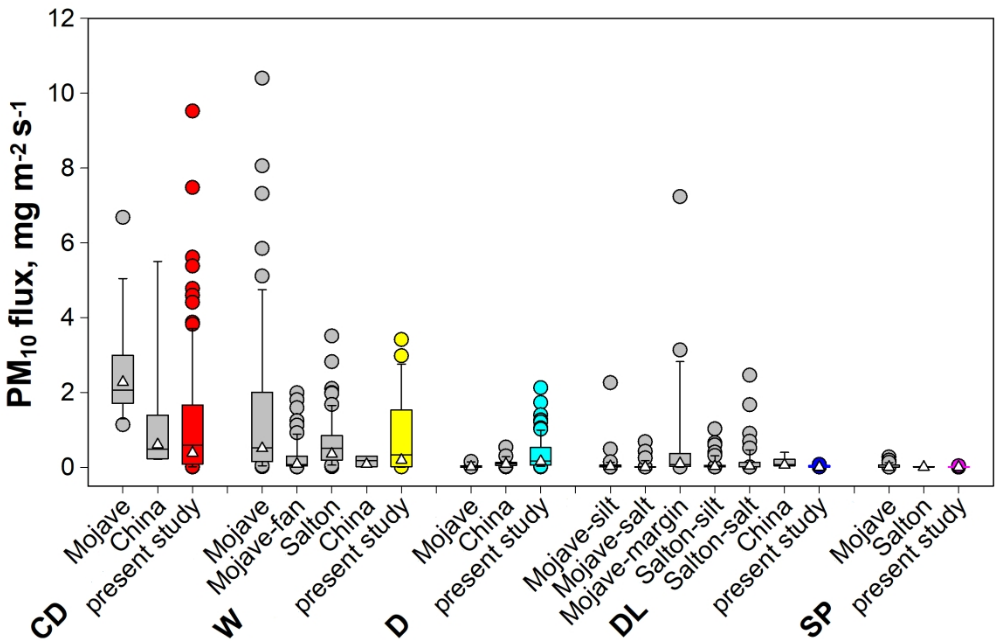

Figure 7. Box plot comparing PM10 fluxes from different landform types measured in the present study with other published PI-SWERL data at u*=0.55 m s-1. The whiskers and boxes, from top to bottom, denote the 90th, 75th, median, 25th percentiles and 10th percentiles. Top and bottom dots represent maximum and minimum values. The white triangles in boxes denote the geometric means. Landform types: CD-coppice dune, W-wadi, D-dune, DL-dry lake, SP-stone pavement. Mojave-fan denotes distal alluvial fan. Dry lake sites in the Mojave Desert and the Salton Sea are classified into subgroups based on crust types (e.g. silt-clay and salt) and location (i.e. margin). Published data are from the Mojave Desert (Macpherson et al., 2008; Sweeney et al., 2011) and the Salton Sea, USA (Sweeney et al., 2008, 2011; King et al., 2011) as well as our prior study in China (Cui et al., 2015; Sweeney et al., 2016).

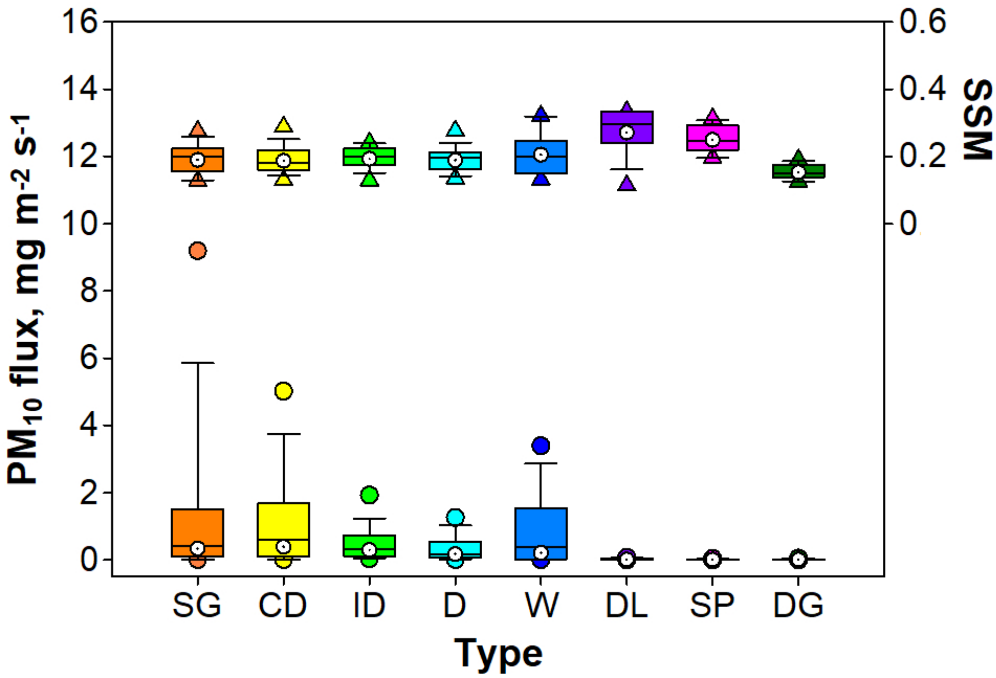

Figure 8. Box plot comparing measured PM10 fluxes at u*= 0.55 m s-1 from different landform types across all seasons and corresponding values from the sediment supply map (SSM) of Parajuli and Zender (2017). The whiskers and boxes, from top to bottom, denote the 95th, 75th, median, 25th percentiles and 5th percentiles. Top and bottom dots/triangles represent the maximum and minimum values. The white circles with dots in boxes denote the geometric means. Landform types: SG-sparse grassland, CD-coppice dune, ID-interdune, D-dune, W-Wadi, DL-dry lake, SP-stone pavement, DG-dense grassland.

Supplementary material for

Quantifying the effect of geomorphology on aeolian dust emission potential in northern China

Mengchun Cui[1,2], Huayu Lu[1*], Giles F.S. Wiggs[2], Vicken Etyemezian[3], Mark R. Sweeney[4], Zhiwei Xu[1]

[1]School of Geography and Ocean Science, Nanjing University, Nanjing, China

[2]School of Geography and the Environment, University of Oxford, Oxford, UK

[3]Division of Atmospheric Science, Desert Research Institute, Las Vegas, Nevada, USA

[4]Department of Sustainability & Environment, University of South Dakota, Vermillion, South Dakota, USA

*Correspondence to: Huayu Lu, huayulu@nju.edu.cn. Tel.: +86 25 89680798; fax: +86 25 89682686.

List of tables.

List of figures.

Table S1. The land use classification system, modified after Liu et al., 2005.

1st level classes		2nd level classes[a]		
Code	Name	Code	Name	Descriptions
1	Cropland	–	–	Cultivated lands for crops. Including: mature cultivated land, newly cultivated land, fallow and shifting cultivated land; intercropping land such as crop-fruiter, crop-mulberry, and crop-forest land in which a crop is a dominant species; bottomland and beach that cultivated for at least 3 years.
2	Woodland	–	–	Lands growing trees including arbor, shrub, bamboo and for forestry use.
3	Grassland	–	–	Lands covered by herbaceous plants with coverage greater than 5%, including shrub rangeland and mixed rangeland with the coverage of shrub canopies less than 10%.
		31	Dense grass	Grassland with canopy coverage greater than 50%.
		32	Moderate grass	Grassland with canopy coverage between 20% and 50%.
		33	Sparse grass	Grassland with canopy cover between 5% and 20%.

4	Water body	–	–	Lands covered by natural water bodies or lands with facilities for irrigation and water reservation.
5	Built-up land	–	–	Lands used for urban and rural settlements, factories and transportation facilities.
6	Unused land	–	–	Lands that are not put into practical use or difficult to use.
		61	Sandy land	Sandy land covered with less than 5% vegetation cover.
		62	Gobi	Gravel covered land with less than 5% vegetation cover.
		63	Salina	Lands with salina accumulation and sparse vegetation.
		64	Swampland	Lands with a permanent mixture of water and herbaceous or woody vegetation that cover extensive areas.
		65	Bare soil	Bare exposed soil with less than 5% vegetation cover.
		66	Bare rock	Bare exposed rock with less than 5% vegetation cover.
		67	Others	Other lands such as alpine desert and tundra.

[a]The 2nd classes of the cropland, woodland, water body and build-up land are not present.

Table S2. The values of α applied in this study.

Type	α
Sparse grassland	0.90
Coppice dune, interdune, dune, dry wash	0.96-0.90[a]
Dry lake	0.98 (silt-clay crusted) or 0.86 (salt crusted)
Stone pavement	0.86
Dense grassland	0.84
Disturbed surface	0.98

[a]Based on the negative relationship with the grain size. For example, a value of 0.96 was applied for those with mean grain size (Md) within 100-200 μm. The value of α decreased by 0.02 with the span of the Md increasing 100 μm.

Table S3. Soil textural characteristics of test sites.

Type	Sand	Loamy sand	Sandy loam
Sparse grassland	90%	10%	
Coppice dune, interdune[a], dune	100%		
Wadi	88%	6%	6%
Dry lake	77%	8%	8%
Stone pavement	31%	23%	46%
Dense grassland	50%	39%	11%

[a]Two interdune sites that were covered with crust were classified as sandy loam and loam. These results were not presented in this table.

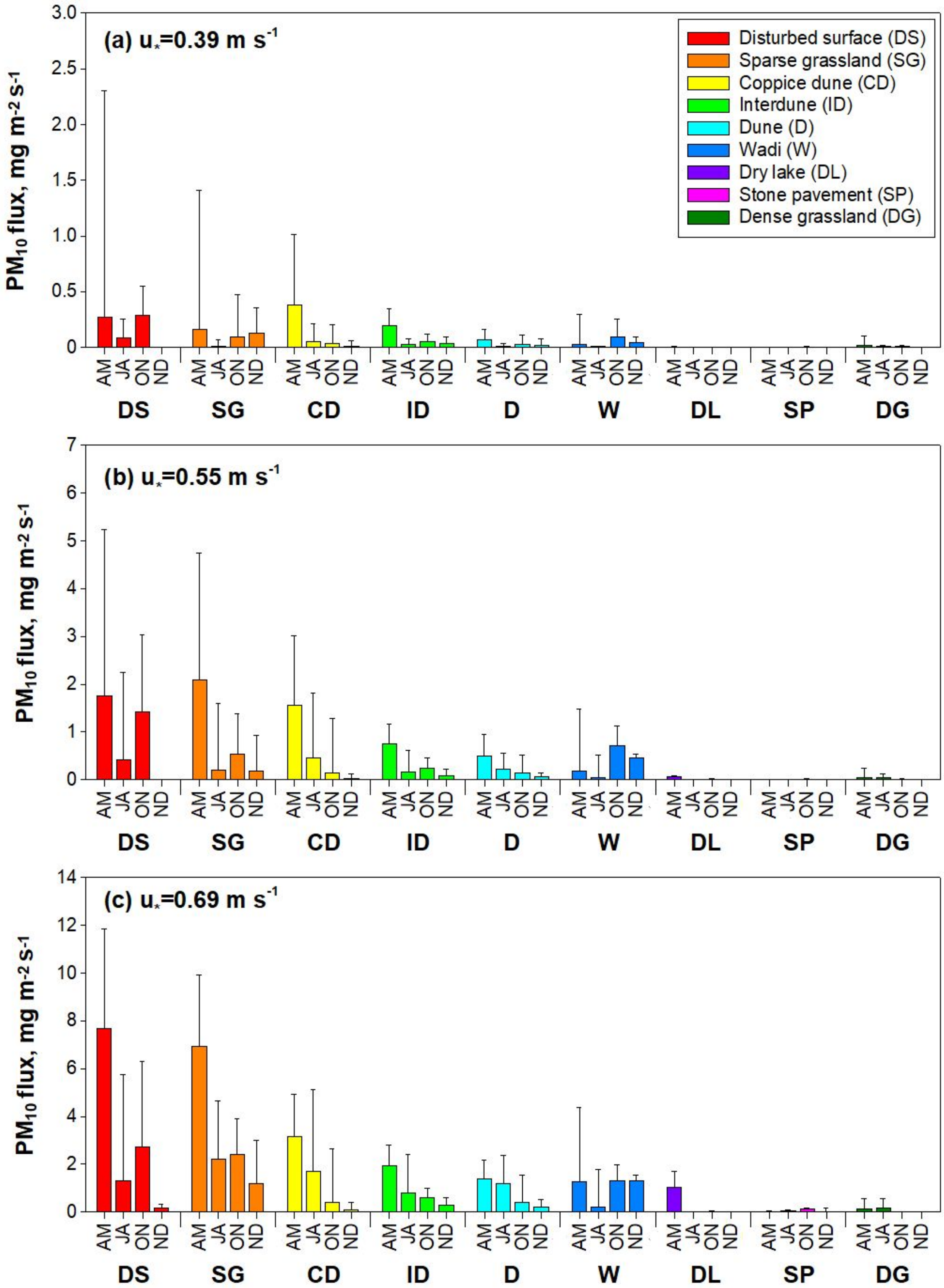

Figure S1. Geometric means and standard deviations of PM_{10} fluxes for different landform types during April-May (AM), July-August (JA), October-early November (ON) and late November-December (ND).

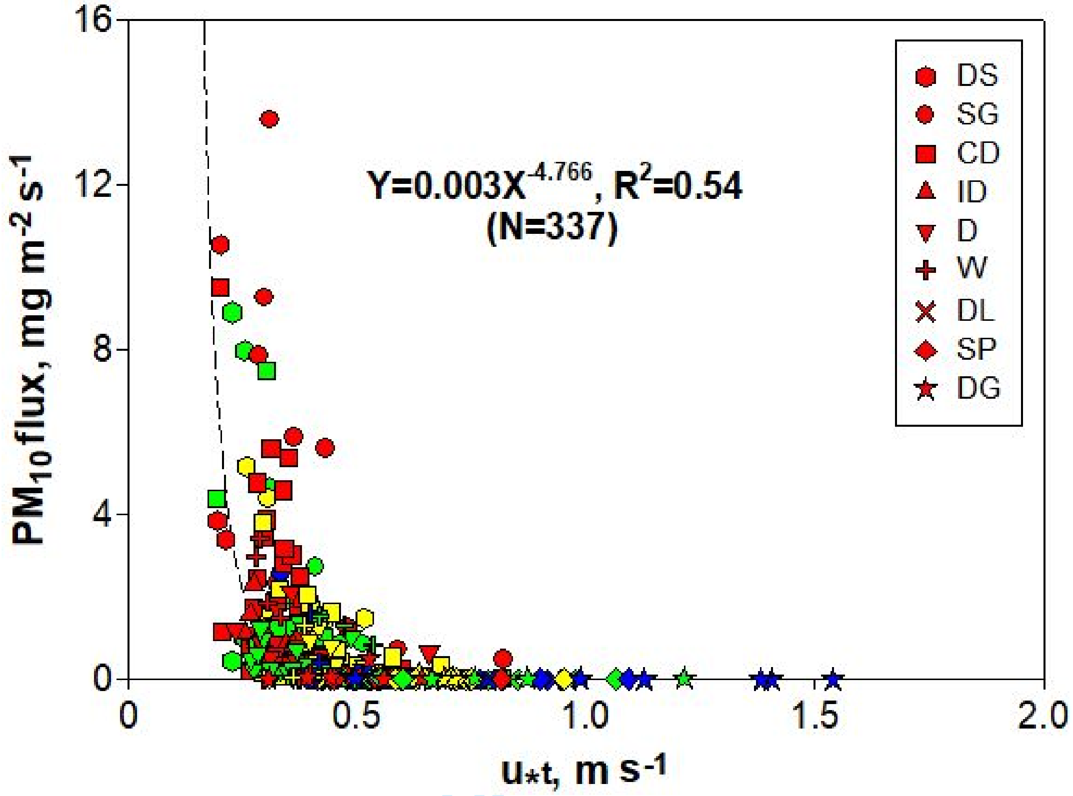

Figure S2. Regression analysis of the relationship between PM_{10} flux at u_*=0.55 m s^{-1} and u_{*t} for all sites in AM (red), JA (yellow), ON (green), and ND (blue). DS-disturbed surfaces, SG-sparse grassland, CD-coppice dune, ID-interdune, D-dune, W-wadi, DL-dry lake, SP-stone pavement, DG-dense grassland.

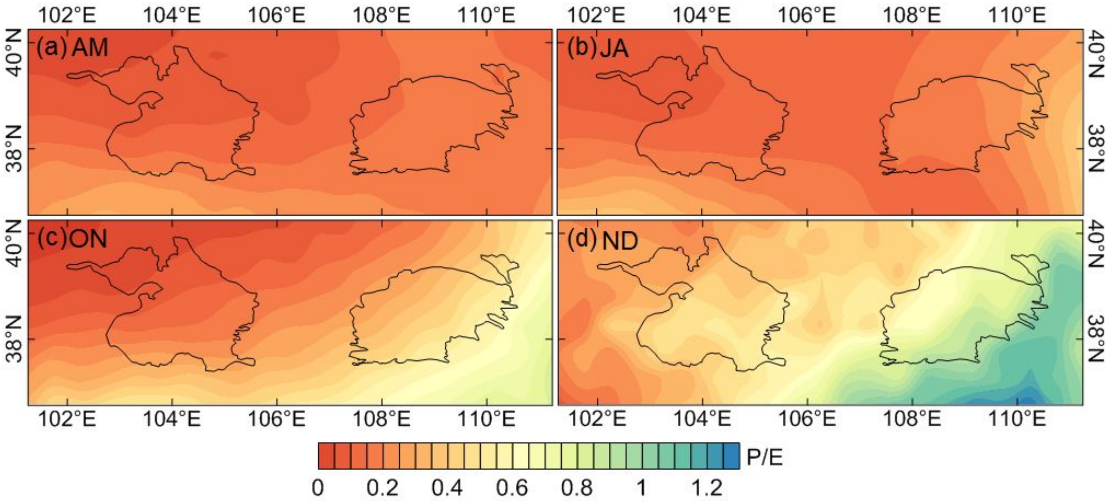

Figure S3. Spatial distribution of the ratio of precipitation to evapotranspiration during test periods (0.5°×0.5°), derived from the monthly high-resolution gridded dataset produced by the Climatic Research Unit.

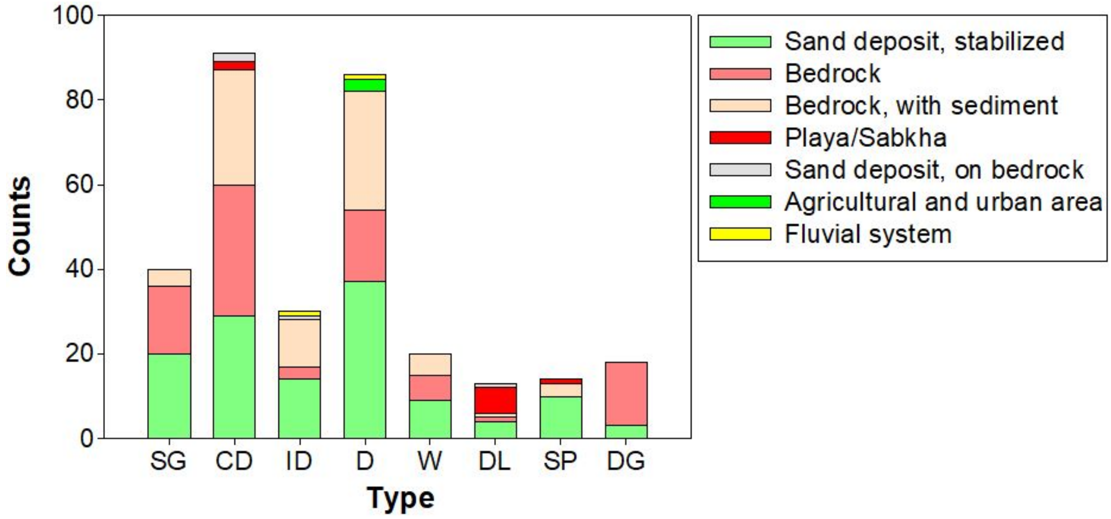

Figure S4. The land surface classification of all test sites according to the land surface map of Parajuli and Zender (2017). Categories in the legend were rearranged in descending order of site counts. SG-sparse grassland, CD-coppice dune, ID-interdune, D-dune, W-wadi, DL-dry lake, SP-stone pavement, DG-dense grassland.